Nano Materials Science 6 (2024) 635–646

Contents lists available at ScienceDirect

Nano Materials Science

journal homepage: www.keaipublishing.com/cn/journals/nano-materials-science/

Low-frequency and dual-band microwave absorption properties of novel VB-group disulphides (3R–TaS_2) nanosheets

Liquan Fan [a,1], Honglin Ai [a,1], Meiye Jiao [a], Yao Li [a], Yongheng Jin [b], Yiru Fu [a], Jing Wang [a], Yuwei Wang [a], Deqing Zhang [a,**], Guangping Zheng [c], Junye Cheng [b,*]

[a] College of Materials Science and Engineering, Heilongjiang Provincial Key Laboratory of Polymeric Composite Materials, Qiqihar University, No.42, Wenhua Street, Qiqihar, 161006, PR China

[b] Department of Materials Science, Shenzhen MSU-BIT University, Shenzhen, Guangdong Province, 517182, PR China

[c] Department of Mechanical Engineering, Hong Kong Polytechnic University, Hung Hom, Kowloon, Hong Kong, China

ARTICLE INFO

Keywords:
3R–TaS_2
Nanosheets
Electromagnetic wave absorption
Reflection loss

ABSTRACT

As electromagnetic technology advances and demand for electronic devices grows, concerns about electromagnetic pollution intensify. This has spurred focused research on innovative electromagnetic absorbers, particularly chalcogenides, noted for their superior absorption capabilities. In this study, we successfully synthesize 3R–TaS_2 nanosheets using a straightforward calcination method for the first time. These nanosheets exhibit significant absorption capabilities in both the C-band (4–8 GHz) and Ku-band (12–18 GHz) frequency ranges. By optimizing the calcination process, the complex permittivity of TaS_2 is enhanced, specifically for those synthesized at 1000 °C for 24 h. The nanosheets possess dual-band absorption properties, with a notable minimum reflection loss (RL_{min}) of −41.4 dB in the C-band, and an average absorption intensity exceeding 10 dB in C- and Ku-bands, in the absorbers with a thickness of 5.6 mm. Additionally, the 3R–TaS_2 nanosheets are demonstrated to have an effective absorption bandwidth of 5.04 GHz (3.84–8.88 GHz) in the absorbers with thicknesses of 3.5–5.5 mm. The results highlight the multiple reflection effects in 3R–TaS_2 as caused by their stacked structures, which could be promising low-frequency absorbers.

1. Introduction

In modern communication and defense systems, electromagnetic wave (EMW) absorbing materials have attracted attention due to their crucial role in reducing electromagnetic interference and enhancing the stealth and safety of electronic devices [1–4]. With the rapid advancement of wireless communication technologies, the demand for efficient EMW absorbing materials is rapidly growing, especially in the areas of low-frequency [5] and dual-band applications [6]. The research on EMW absorbing materials focuses not only on improving absorption rates but also on achieving light weight, thin thickness, and broad bandwidth coverage. Despite the exploration of a variety of materials for microwave absorption, its is a grand challenge that all these characteristics are achieved comprehensively.

Transition metal disulfides (TMDs), owing to their unique electronic structures and physical properties, have demonstrated significant potential for applications in EMW absorption [7–10]. In particular, TMDs with transition metals of VB group, such as vanadium disulfide (VS_2) [6, 11–14] and niobium disulfide (NbS_2) [15–18], have shown their effectiveness in controlling EMW propogation and absorption. Coaxially stacked VS_2 nanosheets (CSVNs), prepared via a simple one-step hydrothermal method, have shown good absorption performance in both the C-band (4–8 GHz) and Ku-band (12–18 GHz) [6]. The VS_2/NiO composite, formed by uniformly attaching nickel oxide (NiO) onto VS_2 nanosheets, exhibited significant EMW absorption effects [11]. Moreover, through coating biomass-derived glucose carbon (GDC) onto stacked VS_2 nanosheets and treating the VS_2/GDC composite by high-temperature carbonization, the effective absorption bandwidth and environmental stability of the composite material were significantly enhanced [12]. NbS_2 is a novel TMD that has been developed for EMW absorption. For instance, NbS_2 nanosheet-based EMW absorbers, prepared via a simple one-step solvothermal method, achieved a tunable

* Corresponding author.
** Corresponding author.
E-mail addresses: 00582@qqhru.edu.cn (D. Zhang), chengjunye@smbu.edu.cn (J. Cheng).

[1] Liquan Fan and Honglin Ai contribute equally to this work.

https://doi.org/10.1016/j.nanoms.2024.05.011
Received 2 April 2024; Accepted 14 May 2024
Available online 31 May 2024

frequency band [16]. Meanwhile, the electromagnetic properties of NbS_2 were successfully modulated by intercalating transition metals (Fe, Co, Ni) [17], tuning their EMW absorption properties. Hu et al. [19] synthesized d-$Mo_2TiC_2T_x$ MXene through a combination of HF acid etching and intercalation layer delayering, enhancing the synergistic effect of dielectric-magnetic loss and matching impedance in a 2D/2D structure with multiple scattering by supporting Ni through various solvothermal reduction pathways. In addition to metallic materials, non-metallic material adhesives can also serve as ideal materials for high-strength electromagnetic wave absorption. They prepared multifunctional SiC nanofiber aerogel springs (SiC NFAS) via a simple thermochemical process, demonstrating good superelasticity and cyclic fatigue resistance [20]. By utilizing freeze casting technology, followed by carbonization and calcination processes, they successfully synthesized a multifunctional monolithic SiC ceramic aerogel with excellent mechanical properties, ideal impedance matching, and efficient EMW absorption performance [21]. This work paves the way for the development and widespread application of high-strength electromagnetic absorbing materials.

Compared to other VB-group TMDs, tantalum disulfide (TaS_2) exhibits unique advantages in EMW absorption due to its distinctive electronic structure, phase transition characteristics, dielectric loss capabilities, chemical and thermal stability, as well as its adjustable interlayer spacing and layered structure [22–32]. However, current research on TaS_2 in the EMW absorption filed primarily focuses on those with 1T or 2H phase, mostly utilizing commercial TaS_2 for the modification of compositions of microwave absorbing materials, with very few studies on the fabrication process of TaS_2. Wan et al. [33] reported the preparation and EMW absorption of ultra-thin 1T-TaS_2/Co(Cp)$_2$ microwave absorbing materials through mixing TaS_2/Co(Cp)$_2$ superlattice. The dynamic Ta═Co dipoles, dielectric matching and ferromagnetism under high dielectric constants were achieved in 1T-TaS_2/Co(Cp)$_2$, thereby enhancing their microwave absorption performance. Sun et al. [34] studied re-stacked 2H–TaS_2 nanosheets resulting from the van der Waals interactions in an intercalated manner, which were then combined with polymer fibers to improve their electrical conductivity and electromagnetic interference shielding effectiveness. These studies mainly focus on the wave absorption and shielding properties of TaS_2 composites, while there has been no report on the fabrication process and EMW absorption performance of the unmodified TaS_2 with a 3R phase. Therefore, in this work, we develop TaS_2 nanosheets with a substantial amount of 3R phase as a microwave absorbing material for the first time. By adjusting the reaction temperature and shortening the reaction time, the nanosheets are found to exhibit exceptional EMW absorption performance, particularly in the C band, showing a minimum reflection loss of −41.4 dB. Notably, these unblended TaS_2 nanosheets exhibit dual-band absorption characteristics in both the C- and Ku-bands. The abundant active sites and stacked nanosheets of TaS_2 provide multiple reflection interfaces for EMW absorption, offering new possibilities for the development of TaS_2-based EMW absorbers. This work could facilitate a comprehensive understanding on the EMW loss mechanisms in VB-group TMDs absorbers.

2. Experimental details

2.1. Preparation of TaS_2 nanosheet

Firstly, the mass (1.7911 g) of tantalum pentachloride ($TaCl_5$, Shanghai Aladdin Reagent Co., Ltd., China) was measured, serving as a reference for the determination of the requisite dosage of thioacetamide (CH_3CSNH_2, Tianjin Guangfu Fine Chemical Co., Ltd., China. The mass ratio of $TaCl_5$ to CH_3CSNH_2 was 1:2, while additional CH_3CSNH_2 was added to ensure the reaction could be complete. The two substances were transferred to a dry and sealed glove box. The mixed powder was then ground and placed in a tube furnace using a small crucible. The product was heated to 800 °C at a rate of 10 °C min^{-1} in an argon environment and calcined for 12 h. After calcination, the sample was ground into a black powder using a mortar, and the resulting sample was named TaS_2-12-800. Similarly, samples TaS_2-12-900 and TaS_2-12-1000 were synthesized using the same method with calcination temperatures of 900 °C and 1000 °C, respectively. The TaS_2 samples synthesized at high temperatures could have the 3R phase. For comparison on the influence of calcination time on the samples, some samples were synthesized at 800, 900, and 1000 °C for 24 h and were denoted as TaS_2-24-800, TaS_2-24-900, and TaS_2-24-1000.

2.2. Characterizations

The analysis was performed using a Nippon Rigaku Smart Lab Diffractometer (Japan) for X-ray diffraction measurements. Scanning electron microscopy (SEM) and energy-dispersive X-ray spectroscopy (EDS) were carried out on a Hitachi S-3400 instrument (Japan). The morphologies and crystal structures of the as-synthesized products were investigated using a Hitachi H-7650 transmission electron microscope (TEM, Japan) and a high-resolution transmission electron microscope (HR-TEM, FEI Tecnai F20, USA). X-ray photoelectron spectroscopy (XPS) was employed for both qualitative and quantitative analyses of the elements, utilizing an ESCALAB 250Xi instrument of Thermo Company (USA). Nitrogen adsorption and desorption isotherms were analyzed using a Mack ASAP2420 nitrogen adsorption meter (USA). The specific surface area was determined using the Brunauer Emmett Teller (BET) method, while the pore size distribution was calculated using the Barrett Joyner Helena (BJH) model. The electromagnetic absorption effectiveness of the samples in the frequency range of 2–18 GHz was assessed using a coaxial method and a vector network analyzer (VNA, MS-200644A ANRITSU, Japan) was used for the measurement. The absorbers containing 60 wt% paraffin and 40 wt% of TaS_2 samples were prepared and compressed into rings with an inner diameter of 3 mm, an outer diameter of 7 mm, and a thickness of 2 mm. The electrical conductivity of the compressed material was measured at room temperature using the four-probe technique.

3. Results and discussion

The schematic of synthesis of stacked TaS_2 nanosheets is depicted in Fig. 1. $TaCl_5$ is used as the tantalum source and CH_3CSNH_2 is used as the sulfur source for the formation of TaS_2 nanosheets. During the reaction, Ta and S ions are combined to form Ta–S–Ta clusters through covalent bonding. These clusters act as nuclei for the formation of TaS_2 nanosheets, resulting in a stacked nanosheet-like structure with a small thickness and definitive profile. When synthesized at high temperatures, TaS_2 exhibits the characteristics of a 3R-type structure, which is relatively stable.

The composition and structure of 3R–TaS_2 are analyzed using an X-ray diffractometer. As shown in Fig. 2(a and b). The characteristic peaks of 3R–TaS_2 are found at 14.84°, 31.49°, and 55.29°, corresponding to crystal planes (003), (101), and (110), respectively [35,36]. The main diffraction peak of 3R–TaS_2 is sharp and high, indicating that the sample has good purity and crystallinity. It should be noted that there are some oxidation peaks in the 20–30° range for samples TaS_2-12-800, TaS_2-12-900, TaS_2-24-800, and TaS_2-24-900. These peaks correspond to Ta_2O_5 (PDF #71–0639).

The XPS spectra of 3R–TaS_2 are shown in Fig. S1, which provid information about the composition and chemical states of the elements in the samples. The presence of oxygen on the sample surface leads to the formation of Ta_2O_5, which coexists with 3R–TaS_2. With increasing calcination temperature, a large number of nanosheet layers are tightly aggregated, resulting in weakening of the peak intensity for Ta_2O_5. The results reveal the presence of five major elements (Ta, S, C, N, and O). A small amount of impurities, N and C, are detected in the sample, which could be attributed to the thermal decomposition of CH_3CSNH_2 during preparation and the formation of residual elements C and N on the

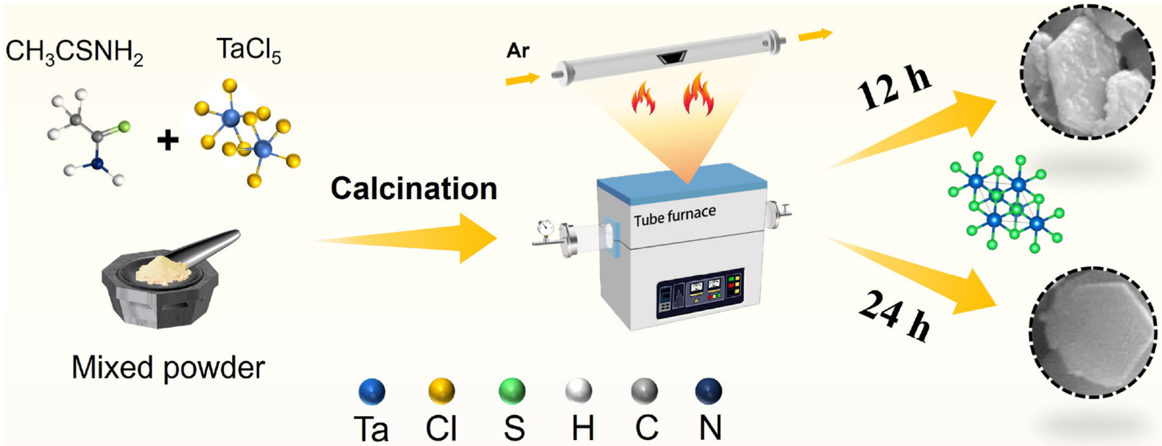

Fig. 1. Preparation process of 3R–TaS_2.

sample surface. Fig. 2(c and d) clearly shows the high-resolution XPS spectra of Ta and S, providing information about their content and chemical states [37,38]. Due to the susceptibility of the TaS_2 powder surface to oxidation, a strong peak of Ta^{5+} belonging to Ta_2O_5 is observed in Fig. 2(c), indicating that Ta^{5+} exists in oxide impurities on sample surface only [39], while Ta^{4+} is attributed to TaS_2 [35]. In order to analyze the specific surface area and pore size distribution of TaS_2, we conducted N_2 adsorption and desorption isotherms along with pore size tests, as illustrated in Fig. S2. The isotherms and hysteresis lines of TaS_2-12-800, TaS_2-12-900, TaS_2-12-1000, TaS_2-24-800, TaS_2-24-900, and TaS_2-24-1000 demonstrate IV-type behavior, indicating the presence of mesoporous pores. Specifically, TaS_2-24-1000 exhibits a pore size concentration at 4.77 nm, with the mesoporous structure significantly enhancing the material's specific surface area to 113.2 $m^2\ g^{-1}$. Furthermore, this mesoporous structure also contributes positively to the material's ability to attenuate electromagnetic waves.

The topography of the TaS_2 nanosheets is examined using scanning electron microscopy (SEM) and transmission electron microscopy (TEM). In Fig. 3(a), the TaS_2-12-1000 nanosheets display a lamellar polygonal structure, and the mapping images (Fig. 3(b and c)) confirm the uniform distribution of elements. As the calcination temperature is increased and the calcination time is extended, the morphology of nanosheets are gradually transformed into a stacking mode, forming a structure that promotes multiple reflections and repeated absorption of electromagnetic waves. Similar polygonal morphological characteristics are observed in TaS_2-24-1000 (Fig. 3(d–f)). Previous studies have discussed the crystal growth mechanisms of the samples, suggesting that the sheet growth mechanism may not be influenced by the movement of the layer faults during growth. In 3R–TaS_2, the Ta atom is coordinated with six S atoms. When there is an excess of Ta atoms, lattice expansion occurs along the stacking direction, leading to a change in the distance between adjacent Ta–S atoms [40,41] and consequently altering the TaS_2 morphology (Fig. 3(g and h)). The lattice spacing of the TaS_2 samples is analyzed using high-resolution TEM (HRTEM) methods, revealing a regular arrangement of TaS_2 layers with a layer spacing of 0.68 nm (Fig. 3(i)). To obtain more accurate inter-layer spacing (d values) corresponding to the crystal planes as estimated from X-ray diffraction analysis, the d values of TaS_2 in Fig. 3(j) are determined by HRTEM to be 0.27 nm, and 0.28 nm, respectively, corresponding to the (012), and (101) crystal planes of 3R–TaS_2. Fig. 3(k) illustrates the sample characteristics with a lattice spacing of 0.24 nm, corresponding to the (104) crystal facets. HRTEM images demonstrate that 3R–TaS_2 is a highly crystalline polycrystalline material.

The EMW absorption performance of microwave-absorbing materials is characterized by the reflection loss (RL), and the electromagnetic compatibility of the as-prepared sample can be evaluated based on the RL value, which is calculated using the formula derived from transmission line theory, as follows [42]:

$$RL = 20 \cdot \log_{10}\frac{|z_{in} - z_0|}{|z_{in} + z_0|} \tag{1}$$

where the normalized input impedance (Z_{in}) is given by:

$$Z_{in} = Z_0\sqrt{\frac{\mu_r}{\varepsilon_r}}\tanh\left(j\left(\frac{2\pi fd}{c}\right)\sqrt{\mu_r\varepsilon_r}\right) \tag{2}$$

where Z_{in} represents the normalized input impedance of the absorber, Z_0 represents the free space impedance, d is the thickness of the absorber, c is the speed of light in a vacuum, f is the frequency of microwaves, ε_r represents the permittivity and $\varepsilon = \varepsilon' - j\varepsilon''$, μ_r is the relative complex permeability and $\mu = \mu' - j\mu''$.

The relationship between the absorbing layer thickness (t_m) and the corresponding absorption peak frequency (f_m) can be described by a quarter-wavelength (l/4) model with the following formula [43–45]:

$$t_m = \frac{n\lambda}{4} = \frac{nc}{4f_m\sqrt{|\varepsilon_r\mu_r|}}\,(n = 1, 3, 5\ldots) \tag{3}$$

where n is the wavenumber, λ is the wavelength of the microwave.

To better understand the mechanisms of microwave absorption, the simulated thickness of TaS_2 determined using the l/4 model is compared with the actual sample thickness. The results (Fig. 4) reveal that unlike traditional microwave absorbing materials, samples synthesized at 24 h exhibit dual-frequency absorption. Similarly, samples synthesized at 800, 900, and 1000 °C for 12 h also show dual-frequency absorption, but to a lesser extent. The dual-band absorption peaks are observed in the C-band and K_u-band, with the minimum reflection loss shifting from the high-frequency to the low-frequency region as the calcination temperature increased. With these variations, we can find that the sample thickness meets the conditions of one-quarter wavelength.

In this study, we successfully synthesize TaS_2 samples by adjusting the calcination temperature and time. From Fig. 4(a and b), it is observed that the RL levels for TaS_2-12-800 and TaS_2-12-900 samples are below −10 dB at the thickness of 5–5.5 mm, while at other thicknesses, the levels barely reach −10 dB. The results can be attributed to the presence of Ta_2O_5 in the sample, which limits its effectiveness in the low frequency region. As depicted in Fig. 4(c), when the calcination temperature is increased, TaS_2-12-1000 samples with thicknesses varying from 1.5 mm to 5.5 mm show an effective absorption bandwidth of approximately 2.96–12.72 GHz and 13.44–18 GHz, with a minimum reflection loss (RL_{min}) of −29.5 dB. Samples synthesized at an extension of the reaction time are analyzed as well, with results shown in Fig. 4(d and e), revealing

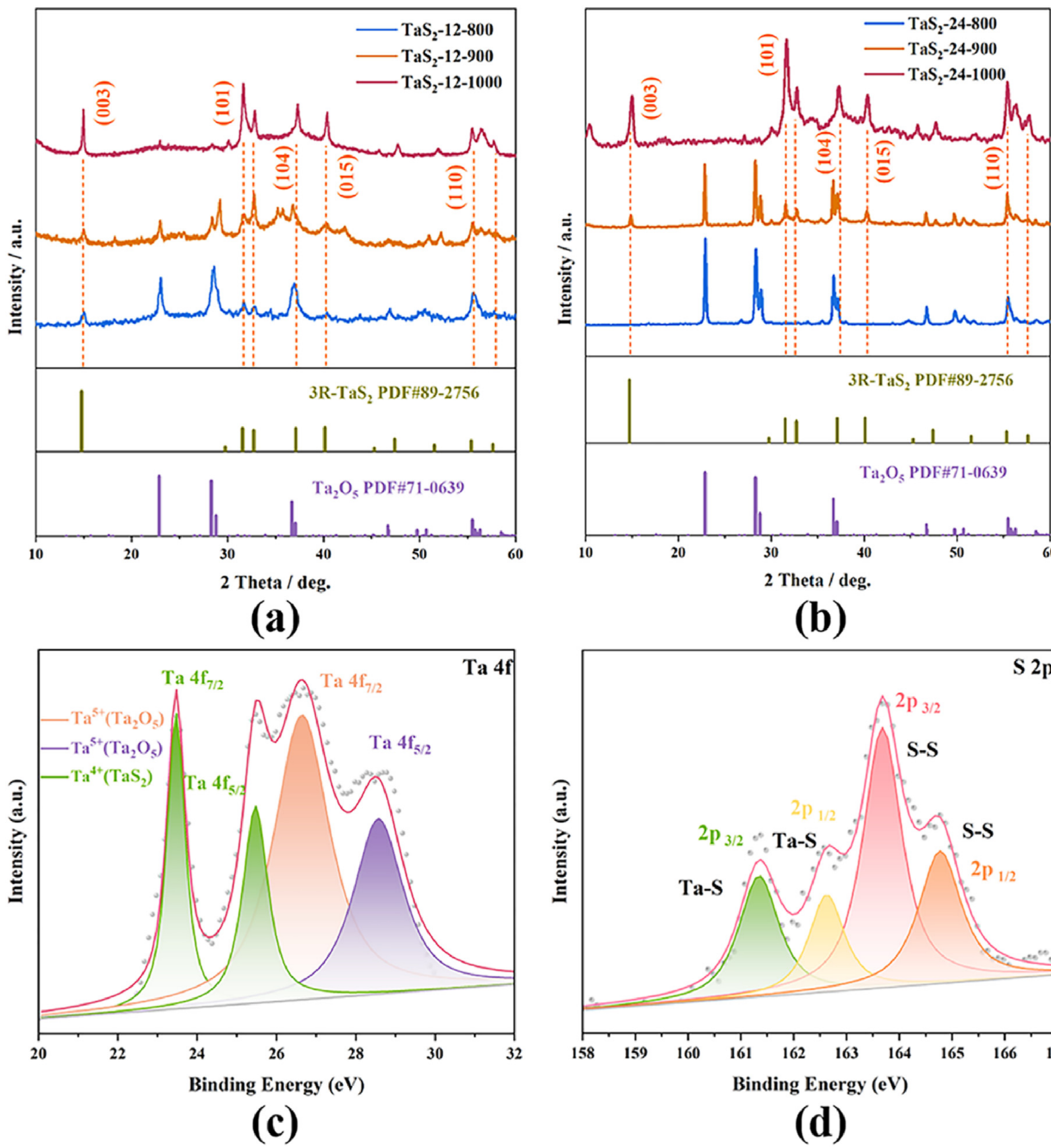

Fig. 2. XRD patterns of (a) TaS_2-12-800, TaS_2-12-900, and TaS_2-12-1000 and (b) XRD patterns of TaS_2-24-800, TaS_2-24-900, TaS_2-24-1000; High-resolution XPS scans of (c) Ta and (d) S.

that the RL_{min} values for TaS_2-24-800 and TaS_2-24-900 samples occurr in the low-frequency region, with values of −25.9 dB and −21.5 dB, respectively. Fig. 4(f) demonstrates that the TaS_2-24-1000 sample achieves an effective absorption bandwidth 3.92–16.56 GHz, with an RL_{min} value of −39.8 dB at a thickness of 5.5 mm. These findings suggest that the optimization on the calcination temperature and time could lead to a dense structure of TaS_2, enhancing interface polarization between Ta_2O_5 and TaS_2 and facilitating charge redistribution, which ultimately improves the capacity for electromagnetic wave absorption.

To further analyze the electromagnetic wave attenuation performance of the samples, the thickness of obsorbers is refined. Fig. 5(a and b) illustrates that RL_{min} of the TaS_2-12-1000 sample, with a thickness ranging from 1.82 to 2.32 mm, reaches −30.6 dB within the 11–11.5 GHz range at a specific thickness of 2.02 mm. Similarly, Fig. 5(c and d) show that the RL level of the TaS_2-24-1000 sample, with a thickness of 5.3–5.8 mm, is as low as −41.4 dB at 4–4.5 GHz at a thickness of 5.6 mm. In summary, as shown in Table 1, the TaS_2 samples developed in this work exhibit excellent electromagnetic wave absorption performance [6, 11–14,16,52–62].

For a deeper examination on the electromagnetic wave absorption process, the material's dielectric properties across a 2–18 GHz frequency spectrum are analyzed, utilizing the following formula [46]:

$$\varepsilon_r = \varepsilon_\infty + \frac{\varepsilon_s - \varepsilon_\infty}{1 + j2\pi f \tau} = \varepsilon' - j\varepsilon'' \quad (4)$$

where ε' is the real part of the complex permittivity, related to the storage capacity of electricity, ε'' is the imaginary part of the complex permittivity, which is related to energy loss.

Based on the data presented in Fig. 6(a) and (d), we observe that the real part of the permittivity, ε', for the TaS_2 EMW absorbing material, decreases with increasing frequency. This trend could be due to the slower response of dipoles at higher frequencies, which leads to reduced storage capacity for electric energy, as indicated by the decrease in ε'. The

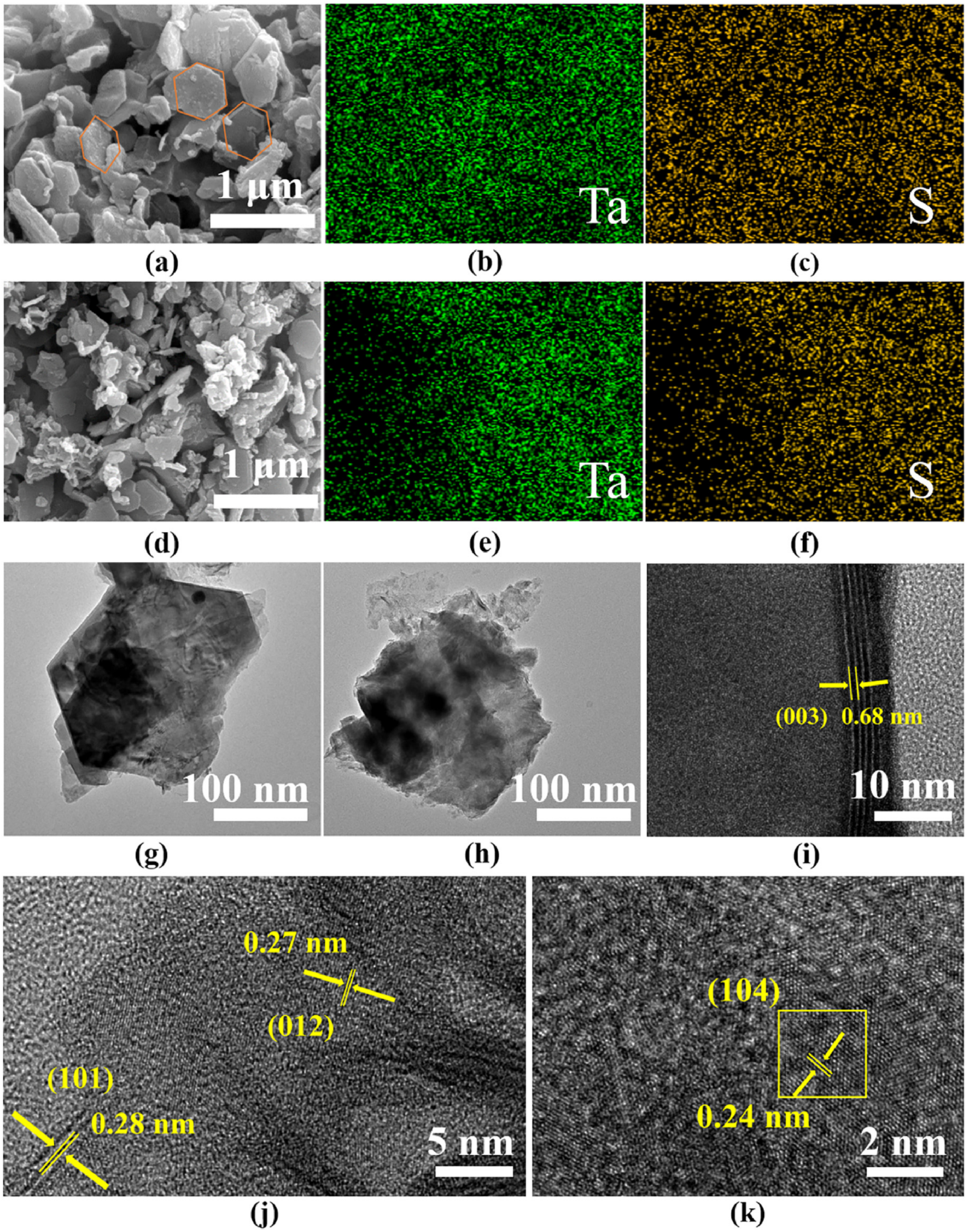

Fig. 3. SEM and TEM images of TaS_2 with corresponding element mapping diagrams: (a) SEM image of TaS_2-12-1000 and the corresponding element mapping diagrams for (b) Ta and (c) S; (d) SEM image of TaS_2-24-1000 and the corresponding element mapping diagrams for (e) Ta and (f) S. TEM images of (g) TaS_2-12-1000 and (h) TaS_2-24-1000. HRTEM images of TaS_2-24-1000 showing the interlayer spacing in regions of 3R–TaS_2: (i), (j), and (k).

results suggests that the attenuation mechanism affecting the RL peak primarily involves polarization relaxation, as indicated by the changes in the imaginary part of the dielectric constant.

In general, the real part of the dielectric constant (ε') represents the material's capacity to store electric energy, while the imaginary part (ε'') indicates how effectively the material can dissipate the energy [47]. Additionally, the ratio of the imaginary part to the real part, known as tangent ($\tan\delta\varepsilon$), is a crucial factor in evaluating the characteristics of the sample. Based on the results shown in Fig. 6(b) and (e), it can be observed that for samples prepared at high reaction temperatures, the imaginary part of the dielectric constant initially increases and then decreases. The comparison between the dielectric constant imaginary part and the reflection loss curve, as depicted in Figs. S3(a–f), indicates an inverse relationship between the RL values and frequency. This suggests that the

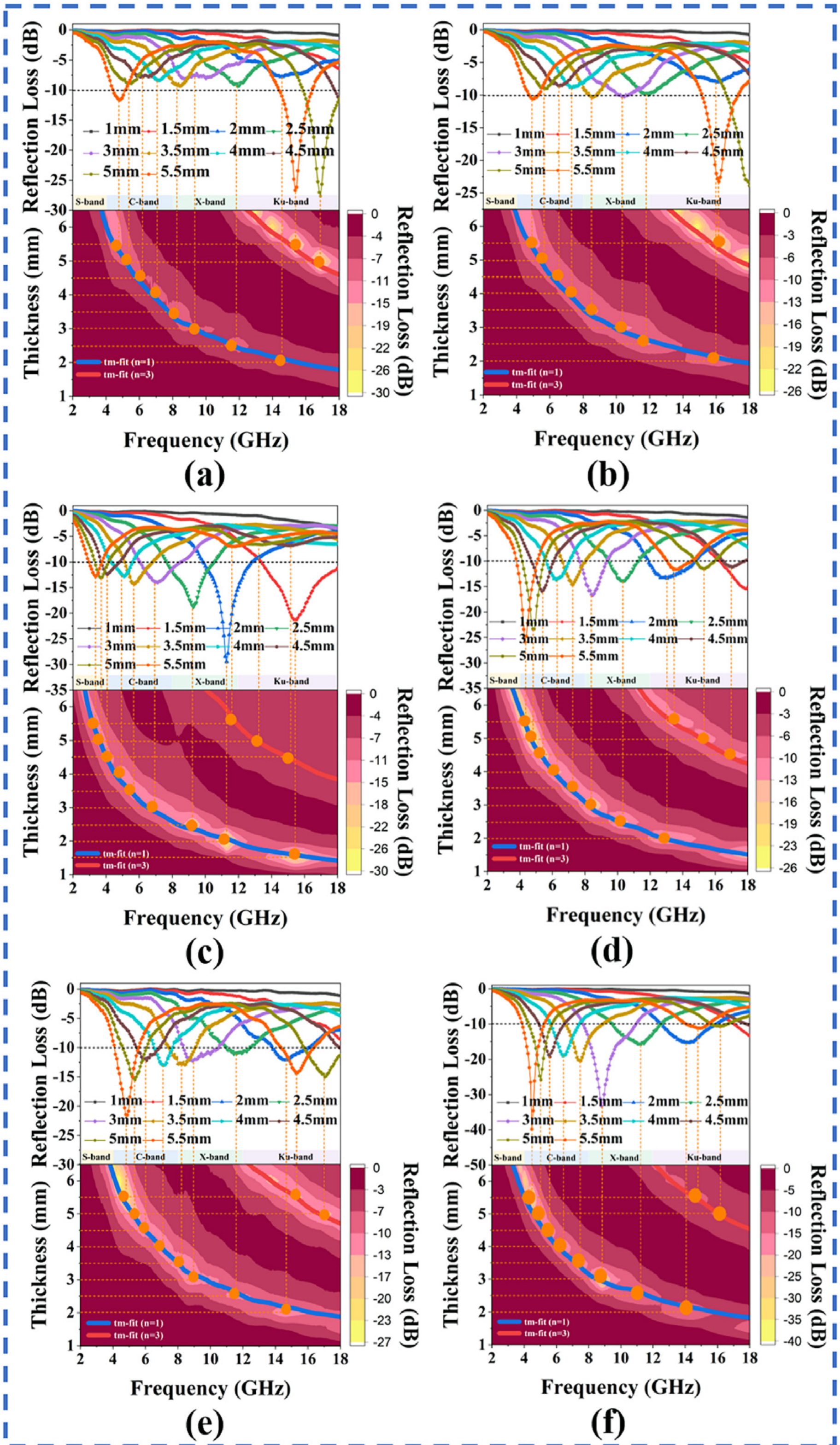

Fig. 4. Reflection loss curves and corresponding quarter-wavelength and three-quarter wavelength matching curves for TaS_2 samples calcined at different temperatures: (a) TaS_2-12-800, (b) TaS_2-12-900, (c) TaS_2-12-1000, (d) TaS_2-24-800, (e) TaS_2-24-900, and (f) TaS_2-24-1000.

attenuation observed during RL measurements is influenced by variations in the imaginary part of the dielectric constant. Notably, TaS_2-12-1000 and TaS_2-24-1000 samples synthesized at a reaction temperature of 1000 °C exhibit a higher dielectric constant. These samples are capable of converting the energy of incident electromagnetic waves into other forms of energy to absorb electromagnetic waves effectively. Hence, it can be concluded that a larger imaginary part of the dielectric constant corresponds to better microwave absorption performance of the sample. Furthermore, as observed in Fig. 6(c) and (f), the $\tan\delta\varepsilon$ values for the TaS_2-12-800, 900, 1000 and TaS_2-24-800, 900, 1000 samples are

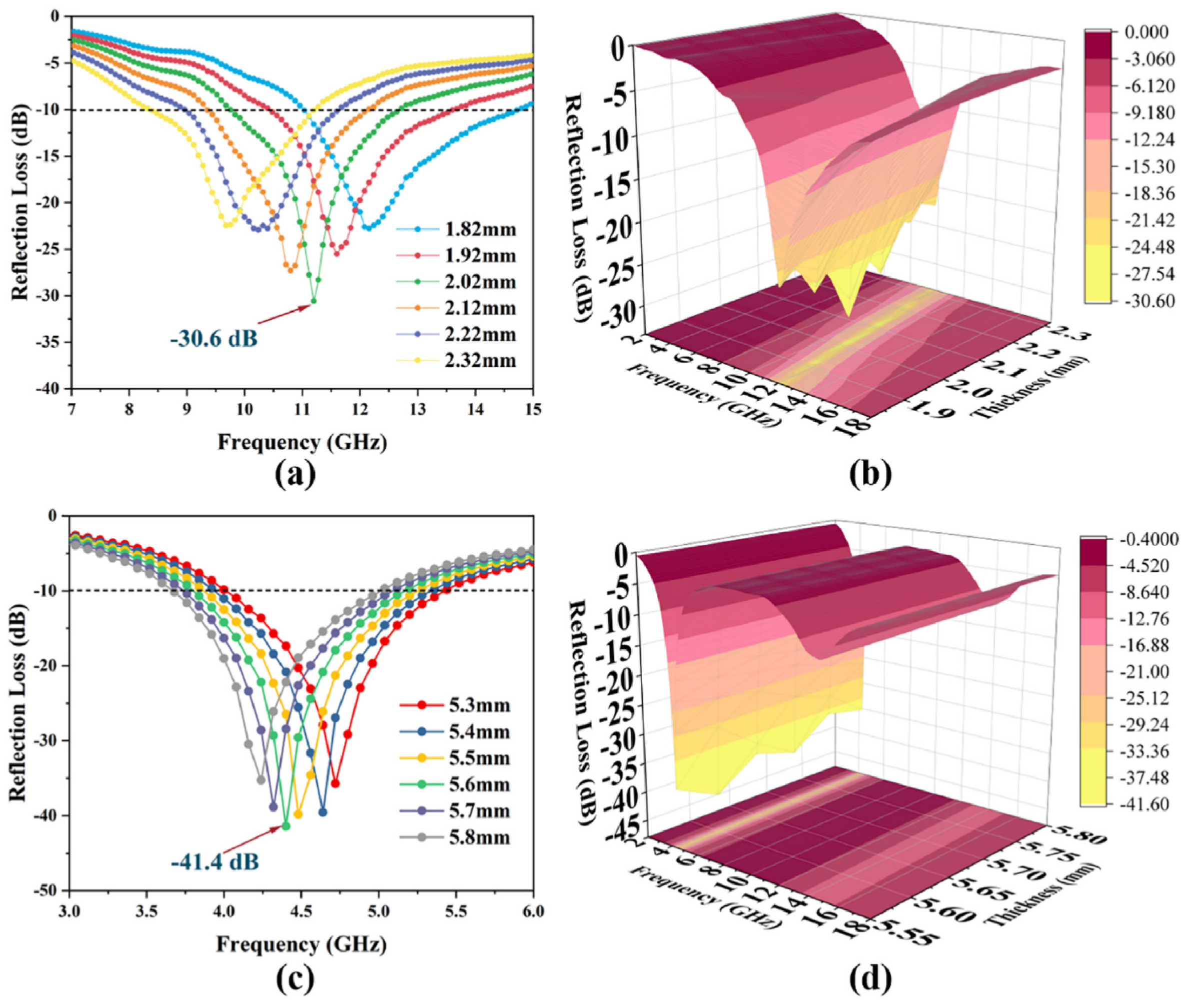

Fig. 5. TaS_2 sample reflection loss (RL) analysis: (a) RL values for TaS_2-12-1000 with thicknesses varying from 1.82 to 2.32 mm; (b) 3D representation of RL changes for the sample in (a); (c) RL values for TaS_2-24-1000 with thicknesses varying from 5.3 to 5.8 mm; (d) 3D representation of RL changes for the sample in (c).

Table 1
Comparative analysis of EMW absorption properties of TMDs prepared in this work and those reported in literature.

Materials	Loading ratio (wt %)	RL (dB)	Frequency (GHz)	Thickness (mm)	RL_{min} (dB)	Frequency (GHz)	Thickness (mm)	Ref.
TaS_2-12-1000	40	−29.5	11.28	2	−30.6	11.2	2.02	This Work
TaS_2-24-1000	40	−39.8	4.48	5.5	−41.4	4.4	5.6	This Work
VS_2	40	−33.8			−57.4	4	5.75	[6]
VS_2–NiO	20			1.5	−58.98	12.32	1.48	[11]
VS_2/GDC	40	−37.4		5.5	−52.8	12.2	2.7	[12]
C/VS_2	75	−54.32	13.4	1.9	−62.74	14.56	1.7	[13]
VS_2/Co_3O_4	40				−57.96	12.8	1.57	[14]
NbS_2	40	−43.5	11.2	2.5				[16]
3D M_OS_2	25	−26.1	11.36	2.5				[52]
WS_2	30	−37	4.3	6	−63	12.1	2.5	[53]
WS_2@BDC	40	−51.4	5.52	4.5				[54]
WS_2/Co	50	−19.8	2.48	4	−46.5	10.2	1.7	[55]
$MoS_2/Ti_3C_2T_x$	96.104	−31.59		5	−61.65		4.53	[56]
C/MoS_2	25	−55.12	12.44	2.06	−75.94	16.2	1.68	[57]
MoS_2/CoS_2/VN	40				−50.48		2.02	[58]
$CoTe_2@MoS_2$	50	−45.8	15	1.6	−68.10	4.71	4.5	[59]
$SiC_f@WS_2$	15	−49.88		2.8	−72.76	12.74	2.86	[60]
MoS_2/Si_3N_4		−31.01	8.47	4.6	−68.66		3.06	[61]
$Si_3N_4@WS_2$		−23.83	8.2	4.94	−65.03	9.17	4.35	[62]

0.20, 0.20, 0.51, 0.30, 0.28, 0.33, respectively, and those samples calcined at 1000 °C for 12 h or 24 h, possess higher $\tan\delta\varepsilon$ values than other samples.

It is suggested that the increase in the imaginary part of the dielectric constant indicates the enhanced electromagnetic wave attenuation, polarization, and relaxation properties of the sample, which could be verified by a detailed analysis on the Debye relaxation process. The relationship between ε' and ε'' can be described by the following formula [48,49]:

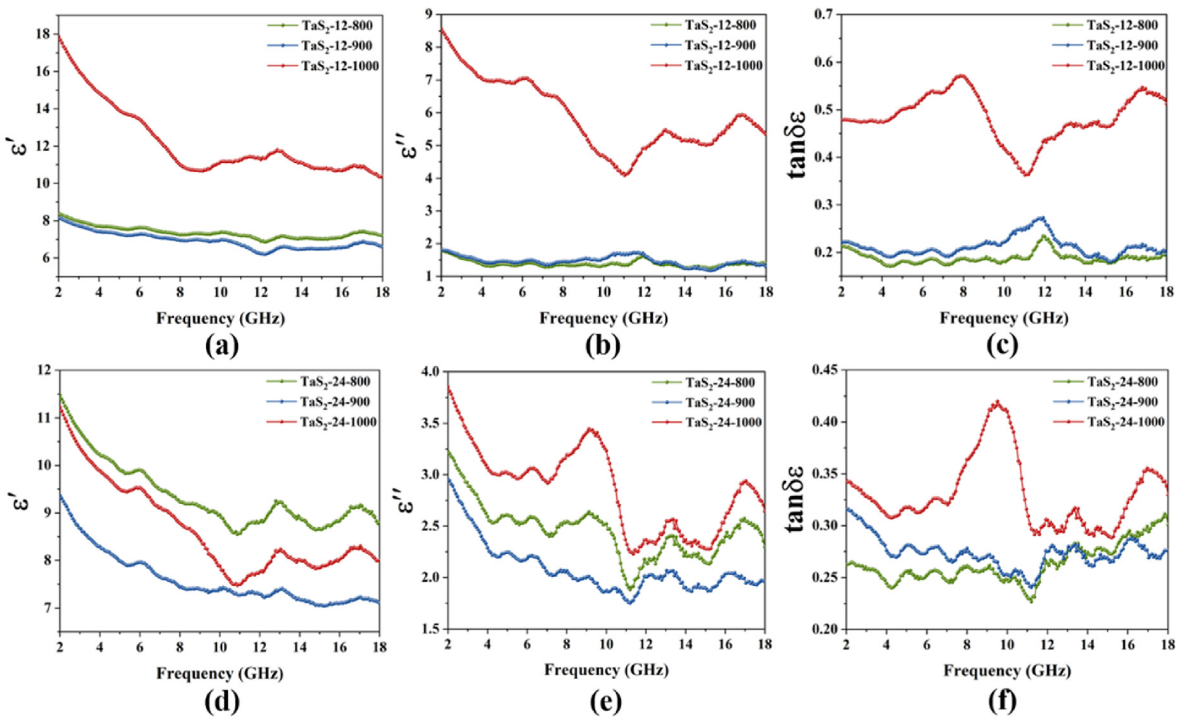

Fig. 6. Dielectric properties of TaS_2 samples: (a) real part and (b) imaginary part of the complex dielectric constant, and (c) dielectric loss tangent for TaS_2-12-800, 900, 1000; (d) real part and (e) imaginary part of the complex dielectric constant, and (f) dielectric loss tangent for TaS_2-24-800, 900, 1000.

$$\varepsilon' = \varepsilon_\infty + \frac{\varepsilon_s - \varepsilon_\infty}{1 + (2\pi f)^2 \tau^2} \quad (5)$$

$$\varepsilon'' = \frac{\varepsilon_s - \varepsilon_\infty}{1 + \omega^2 \tau^2}\omega\tau + \frac{\sigma}{\omega\varepsilon_0} \quad (6)$$

where ω is the angular frequency, f is the frequency, τ is the polarization relaxation time, ε_s is the static permittivity, and ε_∞ is the relative permittivity at infinite frequency. Thus, the relationship between ε' and ε'' is given by the following formula [50]:

$$\left(\varepsilon' - \frac{\varepsilon_s + \varepsilon_\infty}{2}\right)^2 + (\varepsilon'')^2 = \left(\frac{\varepsilon_s + \varepsilon_\infty}{2}\right)^2 \quad (7)$$

In the Cole-Cole plots (Fig. 7(a and b)), each downward semicircle represents a Debye relaxation process, indicating a microwave absorption process. For samples synthesized at reaction temperatures of 800 °C and 900 °C, no Debye relaxation process is evident in the Cole-Cole plots (Fig. S4). However, for the TaS_2-12-1000 samples synthesized at 1000 °C, two Debye-like relaxation processes are observed. In Fig. 7(a), the relaxation of the TaS_2-12-1000 sample occurs at frequencies of 7.6 GHz and 6.2 GHz, which are consistent with the change in frequency shown in the figure for ε'' (dielectric imaginary part). In Fig. 7(b), the TaS_2-24-1000 sample exhibits multiple relaxation processes at frequencies of 9.3 GHz, 7.76 GHz, and 5.84 GHz. The generation of multiple polarization relaxation processes can be attributed to the presence of Ta and S vacancies in the material, which create dipoles at the defect locations, resulting in

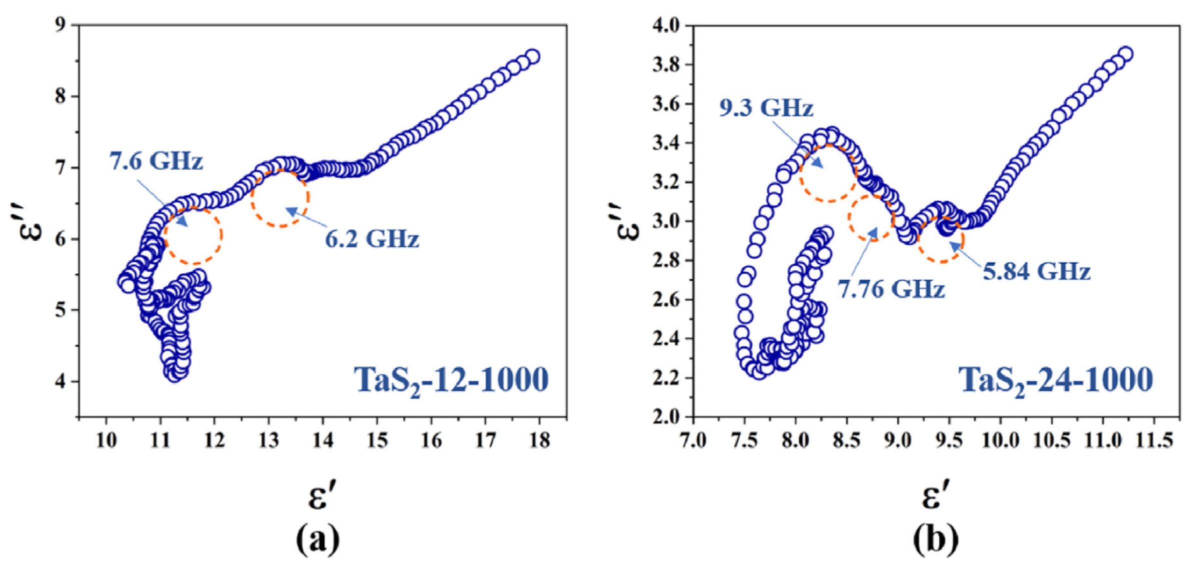

Fig. 7. Cole-Cole curves for TaS_2 samples: (a) TaS_2-12-1000, (b) TaS_2-24-1000.

dipole polarization and attenuation of electromagnetic waves.

A efficient microwave absorber is characterized by its substantial ability to dampen microwave signals. The efficacy of EMW dampening is measured by the attenuation constant (α) as follows [51]:

$$\alpha = \frac{\sqrt{2}\pi f}{c} \times \sqrt{(\mu''\varepsilon'' - \mu'\varepsilon') + \sqrt{(\mu''\varepsilon'' - \mu'\varepsilon')^2 + (\varepsilon'\mu'' + \varepsilon''\mu')^2}} \quad (8)$$

The calculated α is directly compared with the values obtained from experimental data. Notably, the α value for the sample exhibits an increasing trend with increasing frequency. In Fig. S5(a), the α value of TaS_2-12-1000 reaches a maximum value of 267.63, which is greater than those of the samples TaS_2-12-800 and TaS_2-12-900. In Fig. S5(b), the α value of TaS_2-24-1000 reaches a maximum value of 159.59, which is greater than those of the samples TaS_2-24-800 and TaS_2-24-900. It is evident that α values of the samples TaS_2-12-1000 and TaS_2-24-1000 exhibit a rapid growth in the frequency range of 2–10 GHz, indicating their good attenuation performance for EMW absorption. The results are consistent with the those obtained from the RL curves. Based on the analysis discribed above, it can be concluded that the EMW absorption ability of samples TaS_2-12-1000 and TaS_2-24-1000 is related with their calcination time.

Strong absorption loss capacity is a necessary condition for the material to exhibit a significant RL value (in dB), and good impedance matching (M_Z) is the primary condition for EMW to penetrate the absorber. These two values are extremely important electromagnetic wave absorption parameters. According to the theory, when the characteristic impedance Z_{in} of the material is close to the free space impedance Z_0, the electromagnetic radiation can be absorbed to the maximum extent and zero reflection can be achieved on the surface of the material. M_Z can be estimated using the following formula [63]:

$$M_Z = \frac{Z'_{\mathrm{in}}}{|Z_{\mathrm{in}}|^2 + 1} \quad (9)$$

where Z'_{in} is the real part of the normalized input impedance. In general, when M_Z becomes very close to 1, the characteristic impedance matching of the material increases, and specifically, most of the incident electromagnetic waves enter the material.

Through the analysis of the dielectric constant, tan$\delta\varepsilon$, and Cole-Cole curves, it is observed that the samples TaS_2-12-1000 and TaS_2-24-1000 perform well in EMW absorption. Furthermore, the impedance matching is tested for the samples, focusing on determining significant changes in the attenuation constant (α) within the 2–18 GHz range. In Fig. 8(a and b), the impedance matching values of TaS_2-12-800 and TaS_2-12-900 do not reach 1, proving that electromagnetic waves do not enter the material efficiently and the dielectric properties of samples are not improved. In Fig. 8(c), TaS_2-12-1000 exhibits an absorption loss RL close to 1 with the thicknesses of 1.5–5.5 mm, which indicates that the material efficiently absorbs most incident electromagnetic waves and the absorption is maximized without reflection as the waves propagate further. It is worth noting that TaS_2-12-1000 does not achieve perfect impedance matching in the low-frequency region. In contrast, as shown in Fig. 8(d–f), TaS_2-24-1000 achieves a close-to 1 RL value with the thicknesses of 2–5.5 mm and impedance matching is perfectly achived in the low-frequency region. This finding highlights the strong EMW absorption in the low-frequency bands could be achieved in the samples. When the impedance matching is close to 1, the attenuation constant α reaches a maximum value of 159.59, indicating excellent impedance matching and strong electromagnetic wave attenuation ability.

The in-depth investigation of the application of VB-group TMDs with unique physical and chemical properties in EMW absorbing materials is imperative [64]. The attenuation mechanism of stacked TaS_2 nanosheets can be summarized as follows. Firstly, the impedance matching of the absorption system ensures that the incident wave can enter the absorber to its maximum extent. As shown in Fig. 9, when the electromagnetic wave reaches the surface of the TaS_2 nanosheets, it enters the absorber as much as possible. The multi-interface structure of TaS_2 induces dipole and interfacial polarization effects, causing the nanosheets to absorb electromagnetic energy through dipole polarization and polarization relaxation [65]. This leads to multiple reflections and absorption of electromagnetic waves between the material nanosheets, ultimately increasing the propagation path and enhancing the attenuation of internal electromagnetic waves [66]. Furthermore, TaS_2 nanosheets possess good electrical conductivity but still exhibit some resistances. Consequently, the joule heating resulting from currents generated by microwave radiationin in the materials could convert microwave energy

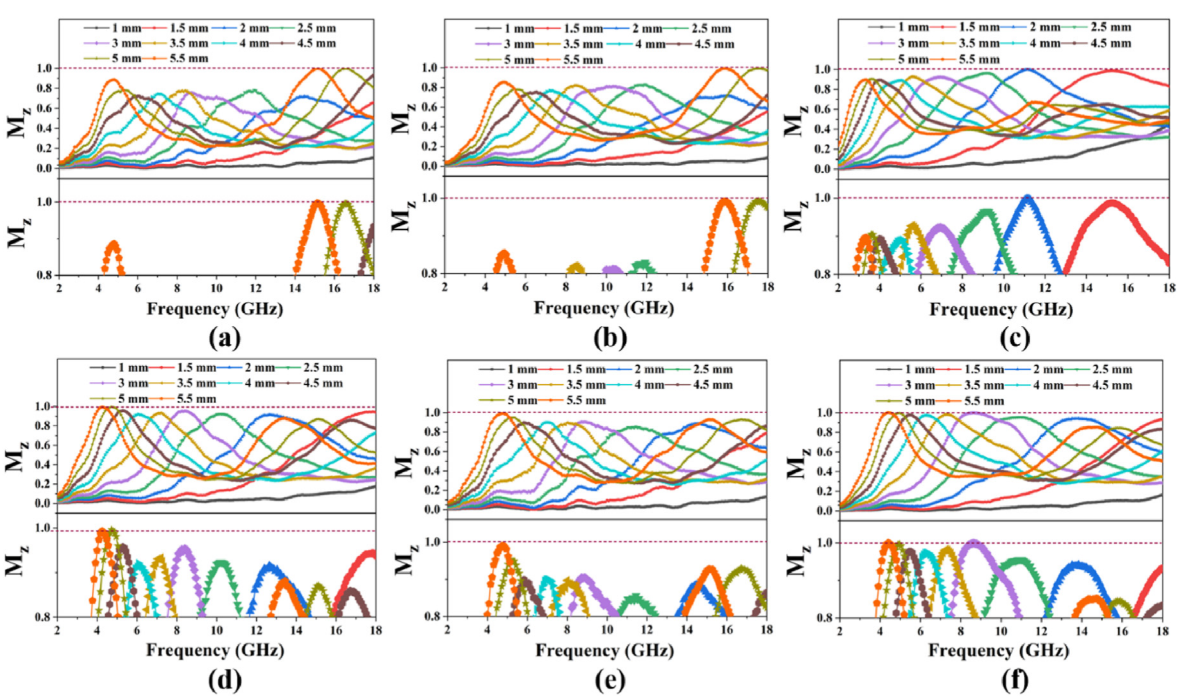

Fig. 8. Impedance matching coefficients of (a) TaS_2-12-800, (b) TaS_2-12-900, (c) TaS_2-12-1000, (d) TaS_2-24-800, (e) TaS_2-24-900, and (f) TaS_2-24-1000.

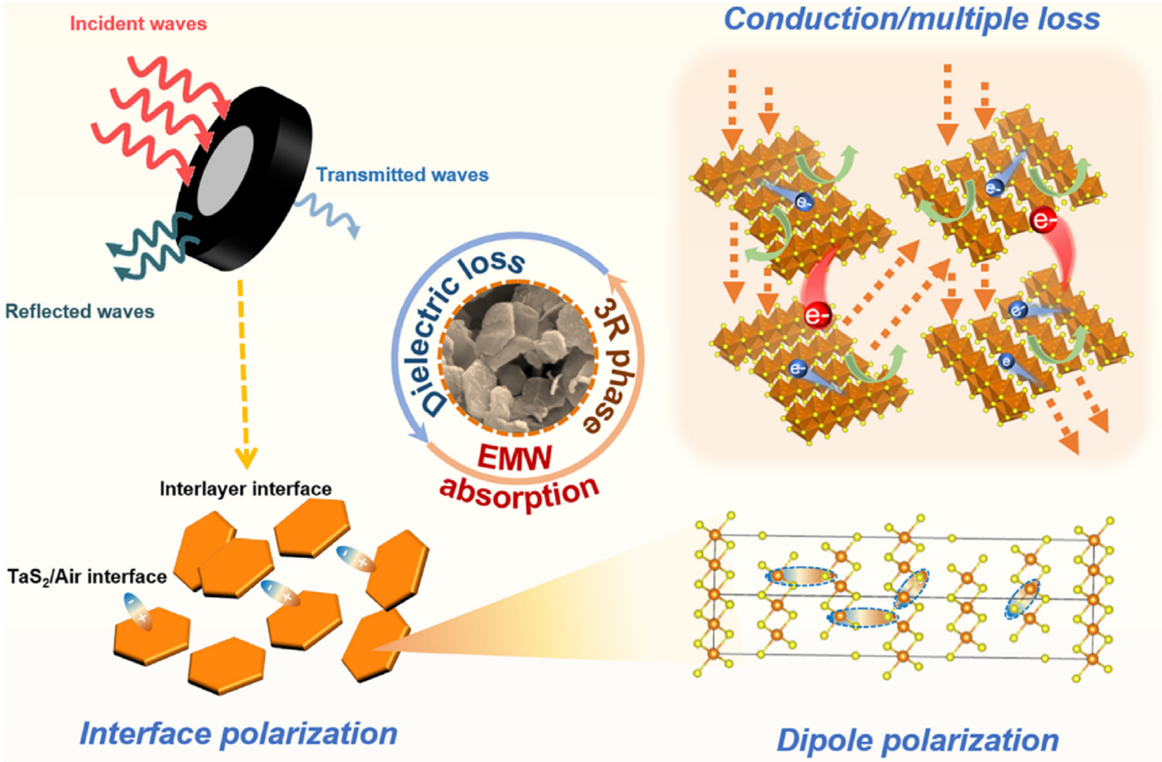

Fig. 9. Schematic diagram of the electromagnetic absorption mechanisms of TaS_2 nanosheets.

into heat energy. Additionally, the electrons generated by microwave radiation can jump between TaS_2 nanosheets, resulting in the dissipation of electromagnetic energy. Therefore, under the synergistic effect of multiple reflections, dipole polarization, and interfacial polarization, TaS_2 nanosheets have excellent EMW absorption performance.

4. Conclusions

In summary, for the first time TaS_2 nanosheets exhibiting outstanding microwave absorption performance are successfully synthesized through a carefully controlled calcination process. By precisely tailoring the thickness of the absorbers, significant microwave absorption across both the C-band and Ku-band is attained. The minimum RL values are exceptionally low, reaching −41.4 dB within the 4–4.5 GHz range. The TaS_2-24-1000 nanosheets, in particular, show superior microwave absorption efficiency, especially within the C-band, demonstrating their promising potential for practical applications. Remarkably, all the TaS_2 nanosheets prepared in this work possess dual-band absorption capability, which is a highly desirable feature for multi-frequency electromagnetic interference shielding. Furthermore, it is revealed that the surface morphology of nanosheets can be tuned by varying the reaction conditions, indicating a controllable synthesis process that could be further optimized. Although the calcination method employed is not novel, the exceptional performance of the resultant TaS_2 nanosheets establishes a solid foundation for the advancements of EMW absorption in TMDs. This work underscores the significant potential of TaS_2-based materials in designing new, efficient composite microwave absorbers.

Declaration of competing interest

The authors declare that they have no known competing financial interests or personal relationships that could have appeared to influence the work reported in this paper.

Acknowledgements

This work was supported by the National Natural Science Foundation of China (52372289, 52102368, 52072192 and 51977009), and Regional Joint Fund for Basic Research and Applied Basic Research of Guangdong Province (No. 2020A1515110905), Guangdong Special Fund for key Areas (20237DZX3042), Shenzhen Stable Support Project.

Appendix A. Supplementary data

Supplementary data to this article can be found online at https://doi.org/10.1016/j.nanoms.2024.05.011.

References

[1] L. Wang, Z.L. Ma, H. Qiu, Y.L. Zhang, Z. Yu, J.W. Gu, Significantly enhanced electromagnetic interference shielding performances of Epoxy nanocomposites with Long-range Aligned lamellar structures, Nano-Micro Lett. 14 (1) (2022) 224.
[2] C.B. Liang, H. Qiu, Y.L. Zhang, Y.Q. Liu, J.W. Gu, External field-assisted techniques for polymer matrix composites with electromagnetic interference shielding, Sci. Bull. 68 (17) (2023) 1938–1953.
[3] D. Mao, Z. Zhang, M. Yang, Z.M. Wang, R.B. Yu, D. Wang, Constructing $BaTiO_3$/TiO_2@polypyrrole composites with hollow multishelled structure for enhanced electromagnetic wave absorbing properties, Int. J. Miner. Metall. Mater. 30 (3) (2023) 581–590.
[4] D.Q. Zhang, S. Liang, J.X. Chai, T.T. Liu, X.Y. Yang, H.H. Wang, J.Y. Cheng, G.P. Zheng, M.S. Cao, Highly effective shielding of electromagnetic waves in MoS_2 nanosheets synthesized by a hydrothermal method, J. Phys. Chem. Solid. 134 (2019) 77–82.
[5] J.L. Liu, L.M. Zhang, D.Y. Zang, H.J. Wu, A Competitive reaction Strategy toward Binary metal sulfides for tailoring electromagnetic wave absorption, Adv. Funct. Mater. 31 (45) (2021) 2105018.
[6] D.Q. Zhang, H.B. Zhang, J.Y. Cheng, H.S. Raza, T.T. Liu, B. Liu, X.W. Ba, G.P. Zheng, G.H. Chen, M.S. Cao, Customizing coaxial stacking VS_2 nanosheets for dual-band microwave absorption with superior performance in the C- and Ku-bands, J. Mater. Chem. C 8 (17) (2020) 5923–5933.
[7] J. Wang, Y.P. Wang, J.Y. Cheng, Y.R. Fu, Y. Li, W.L. Nie, J.W. Wang, B. Liu, D.Q. Zhang, G.P. Zheng, M.S. Cao, Abundant vacancies induced high polarization-

attenuation effects in flower-like WS2 microwave absorbers, J. Mater. Sci. Technol. 194 (2024) 193–202.
[8] J.J. Zhang, X.S. Qi, X. Gong, Q. Peng, Y.L. Chen, R. Xie, W. Zhong, Microstructure optimization of core@shell structured $MSe_2/FeSe_2@MoSe_2$ (M = Co, Ni) flower-like multicomponent nanocomposites towards high-efficiency microwave absorption, J. Mater. Sci. Technol. 128 (2022) 59–70.
[9] J. Yan, Y. Huang, X.Y. Zhang, X. Gong, C. Chen, G.D. Nie, X.D. Liu, P.B. Liu, MoS_2-Decorated/Integrated carbon fiber: phase engineering well-Regulated microwave absorber, Nano-Micro Lett. 13 (1) (2021) 114.
[10] J.K. Liu, Z.R. Jia, W.H. Zhou, X.H. Liu, C.H. Zhang, B.H. Xu, G.L. Wu, Self-assembled MoS_2/magnetic ferrite $CuFe_2O_4$ nanocomposite for high-efficiency microwave absorption, Chem. Eng. J. 429 (2022) 132253.
[11] Z.X. Zhou, X.Y. Yang, D.Q. Zhang, H.B. Zhang, J.Y. Cheng, Y.F. Xiong, Z.H. Huang, H.H. Wang, P. Zhang, G.P. Zheng, M.S. Cao, Achieving superior GHz-absorption performance in VB-group laminated VS_2 microwave absorber with dielectric and magnetic synergy effects, Adv. Compos. Hybrid Mater. 5 (3) (2022) 2317–2327.
[12] H.H. Wang, H.B. Zhang, J.Y. Cheng, T.T. Liu, D.Q. Zhang, G.P. Zheng, S.R. Zhai, M.S. Cao, Building the conformal protection of VB-group VS_2 laminated heterostructure based on biomass-derived carbon for excellent broadband electromagnetic waves absorption, J. Materiomics. 9 (3) (2023) 492–501.
[13] J. Cheng, H.J. Jiang, L. Cai, F. Pan, Y.Y. Shi, X. Wang, X. Zhang, S.D. Lu, Y. Yang, L.X. Li, Z. Xiu, J.L. Wang, H.T. Guo, W. Lu, Porous N-doped C/VB-group VS_2 composites derived from perishable garbage to synergistically solve the environmental and electromagnetic pollution, Chem. Eng. J. 457 (2023) 141208.
[14] Z.H. Huang, J.Y. Cheng, H.B. Zhang, Y.F. Xiong, Z.X. Zhou, Q.B. Zheng, G.P. Zheng, D.Q. Zhang, M.S. Cao, High-performance microwave absorption enabled by Co_3O_4 modified VB-group laminated VS_2 with frequency modulation from S-band to Ku-band, J. Mater. Sci. Technol. 107 (2022) 155–164.
[15] J. Kwak, S. Jung, N. Lee, K. Thiyagarajan, J.K. Kim, A. Giri, U. Jeong, Microwave-assisted synthesis of group 5 transition metal dichalcogenide thin films, J. Mater. Chem. C 6 (42) (2018) 11303–11311.
[16] H.B. Zhang, J.Y. Cheng, H.H. Wang, Z.H. Huang, Q.B. Zheng, G.P. Zheng, D.Q. Zhang, R.C. Che, M.S. Cao, Initiating VB-group laminated NbS_2 electromagnetic wave absorber toward superior absorption bandwidth as large as 6.48 GHz through phase engineering modulation, Adv. Funct. Mater. 32 (6) (2022) 2108194.
[17] L. Gao, M. Li, L.M. Wang, G.Z. Chen, H.X. Yang, B.J. Hu, Q. Huang, Chemical Scissor Medicated intercalation of NbS_2 by transition metal for electromagnetic properties tuning, Adv. Funct. Mater. (2023).
[18] Y. Li, Y.H. Jin, J.Y. Cheng, Y.R. Fu, J. Wang, L.Q. Fan, D.Q. Zhang, P. Zhang, G.P. Zheng, M.S. Cao, Achieving superior electromagnetic wave absorbers with 2D/3D heterogeneous structures through the confinement effect of reduced graphene oxides, Carbon 213 (2023) 118245.
[19] F.Y. Hu, X.H. Wang, S. Bao, L.M. Song, S. Zhang, H.H. Niu, B.B. Fan, R. Zhang, H.X. Li, Tailoring electromagnetic responses of delaminated Mo2TiC2Tx MXene through the decoration of Ni particles of different morphologies, Chem. Eng. J. 440 (2022) 135855.
[20] L.M. Song, B.B. Fan, Y.Q. Chen, Q.C. Gao, Z. Li, H.L. Wang, X.Y. Zhang, L. Guan, H.X. Li, R. Zhang, Ultralight and hyperelastic SiC nanofiber aerogel spring for personal thermal energy regulation, J. Adv. Ceram. 11 (8) (2022) 1235–1248.
[21] L.M. Song, C.W. Wu, Q. Zhi, F. Zhang, B.Z. Song, L. Guan, Y.Q. Chen, H.L. Wang, R. Zhang, B.B. Fan, Multifunctional SiC aerogel reinforced with nanofibers and nanowires for high-efficiency electromagnetic wave absorption, Chem. Eng. J. 467 (2023) 143518.
[22] J.J. Wu, J. Peng, Z. Yu, Y. Zhou, Y.Q. Guo, Z.J. Li, Y. Lin, K.Q. Ruan, C.Z. Wu, Y. Xie, Acid-Assisted Exfoliation toward metallic Sub-nanopore TaS_2 Monolayer with high Volumetric capacitance, J. Am. Chem. Soc. 140 (1) (2018) 493–498.
[23] D. Wang, X. Wang, Y. Lu, C.S. Song, J. Pan, C.L. Li, M.L. Sui, W. Zhao, F.Q. Huang, Atom-scale dispersed palladium in a conductive $Pd_{0.1}TaS_2$ lattice with a unique electronic structure for efficient hydrogen evolution, J. Mater. Chem. A 5 (43) (2017) 22618–22624.
[24] A. Achari, J. Bekaert, V. Sreepal, A. Orekhov, P. Kumaravadivel, M. Kim, N. Gauquelin, P.B. Pillai, J. Verbeeck, F.M. Peeters, A.K. Geim, M.V. Milosevic, R.R. Nair, Alternating Superconducting and charge density wave Monolayers within Bulk 6R-TaS_2, Nano Lett. 22 (15) (2022) 6268–6275.
[25] Z.Y. Wang, Y.Y. Sun, I. Abdelwahab, L. Cao, W. Yu, H.X. Ju, J.F. Zhu, W. Fu, L.Q. Chu, H. Xu, K.P. Loh, Surface-limited Superconducting phase transition on 1T-TaS_2, ACS Nano 12 (12) (2018) 12619–12628.
[26] C.W. Chu, S. Huang, P.D. Hambourger, A.H. Thompson, Pressure effect on the metal-semiconductor transition in 1-T TaS_2, Phys. Lett. (1971).
[27] L.J. Li, W.J. Lu, Y. Liu, Z. Qu, L.S. Ling, Y.P. Sun, Influence of defects on charge-density-wave and superconductivity in 1T-TaS_2 and 2H-TaS_2 systems, Physica. C. 492 (2013) 64–67.
[28] S. Baraghani, Z. Barani, Y. Ghafouri, A. Mohammadzadeh, T.T. Salguero, F. Kargar, A.A. Balandin, Charge-Density-wave thin-Film devices Printed with chemically Exfoliated 1T-TaS_2 Ink, ACS Nano 16 (4) (2022) 6325–6333.
[29] J.Y. Cheng, S.J. Ran, T. Li, M. Yan, J. Wu, S. Boles, B. Liu, H. Raza, S. Ullah, W.J. Zhang, G.H. Chen, G.P. Zheng, Achieving superior tensile performance in individual metal-organic framework crystals, Adv. Mater. (2023) 2210829.
[30] H.L. Chen, J.C. Si, S.L. Lyu, T.Y. Zhang, Z.J. Li, C.J. Lei, L.C. Lei, C. Yuan, B. Yang, L.G. Gao, Y. Hou, Highly effective Electrochemical Exfoliation of Ultrathin tantalum disulfide nanosheets for energy-efficient hydrogen evolution Electrocatalysis, ACS Appl. Mater. Interfaces 12 (22) (2020) 24675–24682.
[31] E. Kovalska, P.K. Roy, N. Antonatos, V. Mazanek, M. Vesely, B. Wu, Z. Sofer, Photocatalytic activity of twist-angle stacked 2D TaS_2, Npj 2D Mater. Appl. 5 (1) (2021) 68.
[32] V. Buravets, F. Hosek, L. Lapcak, E. Miliutina, P. Sajdl, R. Elashnikov, V. Svorcik, O. Lyutakov, Beyond the Platinum Era-Scalable preparation and Electrochemical Activation of TaS_2 flakes, ACS Appl. Mater. Interfaces 15 (4) (2023) 5679–5686.
[33] R.P. Cui, Y. Li, Y.J. Huang, W. Wang, C.L. Wan, Dielectric matching by the unique dynamic dipoles in hybrid organic/Inorganic Superlattices toward Ultrathin microwave absorber, Small 19 (46) (2023).
[34] F.K. Deng, J.H. Wei, Y.D. Xu, Z.Q. Lin, X. Lu, Y.J. Wan, R. Sun, C.P. Wong, Y.G. Hu, Regulating the Electrical and Mechanical Properties of TaS_2 Films via van der Waals and Electrostatic Interaction for High Performance Electromagnetic Interference Shielding, Nano-Micro Lett. 15 (1) (2023) 106.
[35] Y. Feng, S.J. Gong, E.W. Du, X.F. Chen, R.J. Qi, K. Yu, Z.Q. Zhu, 3R TaS_2 Surpasses the corresponding 1T and 2H phases for the hydrogen evolution reaction, J. Phys. Chem. C 122 (4) (2018) 2382–2390.
[36] Y. Feng, S.J. Gong, E.W. Du, K. Yu, J. Ren, Z.G. Wang, Z.Q. Zhu, TaS_2 nanosheet-based ultrafast response and flexible humidity sensor for multifunctional applications, J. Mater. Chem. C 7 (30) (2019) 9284–9292.
[37] P.A. Zong, D.H. Yoo, P. Zhang, Y.F. Wang, Y.J. Huang, S.J. Yin, J. Liang, Y.L. Wang, K. Koumoto, C.L. Wan, Flexible Foil of hybrid TaS_2/organic Superlattice: fabrication and electrical properties, Small 16 (15) (2020) 1901901.
[38] Q.L. Zeng, X. Wang, X.F. Xie, G.H. Lu, Y. Wang, S.C. Lee, J. Sun, TiO_2/TaS_2 with superior charge separation and adsorptive capacity to the photodegradation of gaseous acetaldehyde, Chem. Eng. J. 379 (2020) 122395.
[39] J. Luxa, V. Mazánek, M. Pumera, P. Lazar, D. Sedmidubsky, M. Callisti, T. Polcar, Z. Sofer, 2H → 1T phase engineering of layered tantalum disulfides in Electrocatalysis: oxygen reduction reaction, Chem. Eur J. 23 (33) (2017) 8082–8091.
[40] Y. Gotoh, J. Akimoto, Y. Oosawa, Crystal structure of 3R-$Ta_{1.08}S_2$, J. Alloys Compd. 270 (2) (1998) 115–118.
[41] X.Q. Zhou, C.P. Heinrich, M. Kluenker, S. Dolique, D.L. Mull, C. Lind, Non-hydrolytic sol-gel synthesis of tantalum sulfides, J. Sol. Gel Sci. Technol. 69 (3) (2014) 596–604.
[42] X. Ding, Y. Huang, S.P. Li, N. Zhang, J.G. Wang, 3D architecture reduced graphene oxide-MoS_2 composite: preparation and excellent electromagnetic wave absorption performance, Compos. Part A-Appl. S. 90 (2016) 424–432.
[43] P. Negi, A.K. Chhantyal, A.K. Dixit, S. Kumar, A. Kumar, Activated carbon derived from mango leaves as an enhanced microwave absorbing material, Sustain. Mater. Technol. 27 (2021) e00244.
[44] N. Li, G.W. Huang, Y.Q. Li, H.M. Xiao, Q.P. Feng, N. Hu, S.Y. Fu, Enhanced microwave absorption performance of coated carbon Nanotubes by optimizing the Fe_3O_4 Nanocoating structure, ACS Appl. Mater. Interfaces 9 (3) (2017) 2973–2983.
[45] R.W. Shu, W.J. Li, X. Zhou, D.D. Tian, G.Y. Zhang, Y. Gan, J.J. Shi, J. He, Facile preparation and microwave absorption properties of RGO/MWCNTs/$ZnFe_2O_4$ hybrid nanocomposites, J. Alloys Compd. 743 (2018) 163–174.
[46] B. Zhao, G. Shao, B.B. Fan, Y.J. Xie, R. Zhang, Preparation and electromagnetic wave absorption of chain-like CoNi by a hydrothermal route, J. Magn. Magn Mater. 372 (2014) 195–200.
[47] Y. Shu, T.K. Zhao, X.H. Li, L. Yang, S.Q. Cao, A. Ahmad, T. Jiang, H.J. Luo, Z.M. Jing, N.U. Ain, Flower-like Co@CoO nanohybrids assembled by crisp-rice-like quadrate flakes as high-performance electromagnetic wave absorber, Appl. Surf. Sci. 597 (2022) 153754.
[48] Y.H. Cheng, P. Hu, S.B. Zhou, L.W. Yan, B.Q. Sun, X.H. Zhang, W.B. Han, Achieving tunability of effective electromagnetic wave absorption between the whole X-band and Ku-band via adjusting PPy loading in SiC nanowires/graphene hybrid foam, Carbon 132 (2018) 430–443.
[49] D. Ding, Y. Wang, X.D. Li, R. Qiang, P. Xu, W.L. Chu, X.J. Han, Y.C. Du, Rational design of core-shell Co@C microspheres for high-performance microwave absorption, Carbon 111 (2017) 722–732.
[50] Y.F. Wang, D.L. Chen, X. Yin, P. Xu, F. Wu, M. He, Hybrid of MoS_2 and reduced graphene oxide: a Lightweight and broadband electromagnetic wave absorber, ACS Appl. Mater. Interfaces 7 (47) (2015) 26226–26234.
[51] J. Yan, Y. Huang, X.D. Liu, X.X. Zhao, T.H. Li, Y. Zhao, P.B. Liu, Polypyrrole-based composite materials for electromagnetic wave absorption, Polym. Rev. 61 (3) (2021) 646–687.
[52] X.J. Zhang, S. Li, S.W. Wang, Z.J. Yin, J.Q. Zhu, A.P. Guo, G.S. Wang, P.G. Yin, L. Guo, Self-supported Construction of three-dimensional MoS_2 Hierarchical Nanospheres with tunable high-performance microwave absorption in broadband, J. Phys. Chem. C 120 (38) (2016) 22019–22027.
[53] F. Wu, Y.L. Xia, M.X. Sun, A.M. Xie, Two-dimensional (2D) few-layers WS_2 nanosheets: an ideal nanomaterials with tunable electromagnetic absorption performance, Appl. Phys. Lett. 113 (5) (2018) 052906.
[54] C.X. Hou, J.Y. Cheng, H.B. Zhang, Z.H. Lu, X.Y. Yang, G.P. Zheng, D.Q. Zhang, M.S. Cao, Biomass-derived carbon-coated WS_2 core-shell nanostructures with excellent electromagnetic absorption in C-band, Appl. Surf. Sci. 577 (2022) 151939.
[55] C.L. Li, M.X. Piao, H. Zhang, X. Wang, Constructing of Co nanosheets decorating with WS_2 nanoclusters for enhanced electromagnetic wave absorption, J. Alloys Compd. 912 (2022) 165269.
[56] J.J. Yang, J.Q. Wang, H.Q. Li, Z. Wu, Y.Q. Xing, Y.F. Chen, L. Liu, MoS_2/MXene aerogel with conformal heterogeneous interfaces tailored by atomic layer Deposition for tunable microwave absorption, Adv. Sci. 9 (7) (2022) 2101988.
[57] J. Cheng, L. Cai, Y.Y. Shi, F. Pan, Y.Y. Dong, X.J. Zhu, H.J. Jiang, X. Zhang, Z. Xiang, W. Lu, Polarization loss-enhanced honeycomb-like MoS_2 nanoflowers/undaria pinnatifida-derived porous carbon composites with high-efficient electromagnetic wave absorption, Chem. Eng. J. 431 (2022) 134284.
[58] J.X. Zhou, D. Lan, F. Zhang, Y.H. Cheng, Z.R. Jia, G.L. Wu, P.F. Yin, Self-Assembled MoS_2 Cladding for Corrosion resistant and frequency-modulated electromagnetic wave absorption materials from X-band to K_u-band, Small 19 (52) (2023).

[59] N.X. Zhai, J.H. Luo, P.C. Shu, J. Mei, X.P. Li, W.X. Yan, 1D/2D $CoTe_2$@MoS_2 composites constructed by $CoTe_2$ nanorods and MoS_2 nanosheets for efficient electromagnetic wave absorption, Nano Res. 16 (7) (2023) 10698–10706.
[60] Z.X. Zhao, Z.J. Du, X.Z. Huang, C. Jiang, 1D-2D heterostructured silicon carbide fibers@WS_2 with high efficiency and broad bandwidth for microwave absorption performance, Ceram. Int. 49 (6) (2023) 9916–9923.
[61] J.L. Bai, S.J. Huang, X.M. Yao, X.J. Liu, Z.R. Huang, Surface engineering of nanoflower-like MoS_2 decorated porous Si_3N_4 ceramics for electromagnetic wave absorption, J. Mater. Chem. A 11 (12) (2023) 6274–6285.
[62] J.L. Bai, S.J. Huang, X.M. Yao, X.J. Liu, Z.R. Huang, Core-shell Si_3N_4@WS_2 porous ceramics with improved electromagnetic wave absorption performance, J. Mater. Chem. C (2024).
[63] M. Tang, J.Y. Zhang, S. Bi, Z.L. Hou, X.H. Shao, K.T. Zhan, M.S. Cao, Ultrathin Topological Insulator absorber: unique dielectric behavior of Bi_2Te_3 nanosheets based on conducting surface states, ACS Appl. Mater. Interfaces 11 (36) (2019) 33285–33291.
[64] J.Y. Cheng, Y.H. Jin, J.H. Zhao, Q. Jing, B.L. Gu, J.L. Wei, S.H. Yi, M.M. Li, W.L. Nie, Q.H. Qin, D.Q. Zhang, G.P. Zheng, R.C. Che, From VIB- to VB-group transition metal disulfides: structure engineering modulation for superior electromagnetic wave absorption, Nano-Micro Lett. 16 (1) (2024) 29.
[65] L.M. Song, F. Zhang, Y.Q. Chen, L. Guan, Y.Q. Zhu, M. Chen, H.L. Wang, B.R. Putra, R. Zhang, B.B. Fan, Multifunctional SiC@SiO_2 nanofiber aerogel with Ultrabroadband electromagnetic wave absorption, Nano-Micro Lett. 14 (1) (2022) 152.
[66] L.M. Song, Y.Q. Chen, Q.C. Gao, Z. Li, X.Y. Zhang, H.L. Wang, L. Guan, Z.J. Yu, R. Zhang, B.B. Fan, Low Weight, low thermal Conductivity, and highly efficient electromagnetic wave absorption of Three-Dimensional Graphene/SiC-nanosheets aerogel, Compos Part A-Appl S 158 (2022) 106980.